Cryogenics of a superconducting LINAC: SPIRAL2 from commissioning to operation

Adnan Ghribi,[1,2] Muhammad Aburas,[1,3] Pierre-Emmanuel Bernaudin,[1,3] Patrick Bonnay,[3] François Bonne,[3] Frédéric Bouly,[2] Marco Di Giacomo,[1,3] Charly Lassalle,[1,4] David Longuevergne,[2] François Millet,[3] Jean-Pierre Thermeau,[2] Arnaud Trudel,[1,3] Quentin Tura,[1,2] and Adrien Vassal[1,4]

[1]*Grand Accélérateur National d'Ions Lourds (GANIL), 14000, Caen, France*
[2]*Centre National de la Recherche Scientifique (CNRS), 91400, Orsay France*
[3]*Commissariat à l'Énergie Atomique et aux Énergies Alternatives (CEA), 91400 Saclay, France*
[4]*Université de Caen-Normandie, 14000 Caen, France*

(Received 4 February 2025; accepted 30 July 2025; published 29 August 2025)

The SPIRAL2 superconducting linear accelerator (LINAC), which has been operational since 2019, employs superconducting, independently phased rf resonators to deliver a wide range of particle beams. Designed for flexibility in particle types, intensities, and energies, it utilizes superconducting quarter-wave resonators, the performance of which is critically dependent on the reliability of the cryogenic operation. This paper reviews the evolution of the SPIRAL2 cryogenic system from commissioning to routine operation, which was initially commissioned in 2017. It highlights the key challenges encountered, including thermoacoustic oscillations, thermal management, and the abnormal behavior of cavities. In addition, it explores the integration of thermodynamic modelling and machine learning techniques to enhance system control and diagnose problems. This work serves as a comprehensive resource for advancing cryogenic operations and the performance of superconducting LINACs.

DOI: 10.1103/82xr-d9gc

I. INTRODUCTION

The SPIRAL2[1] linear accelerator (LINAC) is based on superconducting (SC), independently phased rf (radio frequency) resonators. To allow for the wide ranges of particles, intensities, and energies required (see Table I), it is made up of two families of short cryomodules developed by the CEA/Irfu[2] (Saclay) and CNRS/IN2P3/IJCLab[3] teams. The first family, called type A and denoted $A_{i\in[01,12]}$, is composed of 12 quarter-wave resonators (QWRs) optimized for $\beta = 0.07$ (one cavity/cryomodule). The second family, called type B and denoted $B_{i\in[01,07]}$, is composed of 14 QWRs optimized for $\beta = 0.12$ (two cavities/cryomodules) (Fig. 1). The two types of cavities have the same operating temperature of 4.2 K. The resonance frequency was 88.0525 MHz, and the maximum gradient in the operation of the QWRs was $E_{acc} = V_{acc}/\beta\lambda = 6.5$ MV/m. Developed by CNRS/IN2P3/LPSC (Grenoble), rf power couplers provide up to 12 kW of continuous wave (cw) beam loading power to each cavity.

The accelerator has been in operation since August 2019, providing proton and deuteron beams to the Neutrons for Science Facility. The SPIRAL2 cryogenic system is described in detail in [1]. The commissioning of the cryogenic system began in 2017, and it has been operating in the nominal operation mode since 2019. This study aims to provide the community with a general overview of the path from cryogenic commissioning to beam operation. It includes detailed issues such as thermoacoustic oscillations, thermodynamic modeling, LINAC thermal imaging, machine learning-based virtual observers, dynamic heat load compensation, and abnormal behavior of cavities.

The first section describes the constraints and requirements of the cryogenic operation of the SPIRAL2 LINAC. The second section examines the roles of thermodynamic modeling, from control-based to physics-based and machine learning-based inferences of cavity thermal dissipation. The third section details the issues faced during commissioning and operation, as well as how they were diagnosed and mitigated.

[1]https://www.ganil-spiral2.eu
[2]Commissariat à l'Énergie Atomique et aux Énergies Alternatives.
[3]Irène Joliot-Curie Laboratory.

Published by the American Physical Society under the terms of the Creative Commons Attribution 4.0 International license. Further distribution of this work must maintain attribution to the author(s) and the published article's title, journal citation, and DOI.

TABLE I. SPIRAL2 beam specifications. Checked boxes indicate achievements to date. Empty boxes indicate targets not achieved to date.

Particles	H^+		$^3He^{2+}$		D^+		Ions		(Units)
Q/A	1	✓	3/2	✓	1/2	✓	1/3	☐	
Maximum current	5	✓	5	✓	5	✓	1	☐	(mA)
Minimum energy	0.75	✓	0.75	✓	0.75	✓	0.75	☐	(MeV/A)
Maximum energy	33	✓	24	✓	24	✓	15	☐	(MeV/A)
Maximum beam power	165	☐	180	☐	200	☐	45	☐	(kW)

II. CONSTRAINTS AND REQUIREMENTS OF THE CRYOGENIC OPERATION

Cryogenics allow superconducting cavities to reach the required conditions to inject and maintain radio frequency (rf) at the required power level, thereby allowing them to operate at their nominal accelerating gradients.

The first requirement is to maintain the superconducting state of the cavities and ensure that their temperature-dependent surface resistance is uniform. In other words, the system must efficiently extract the rf-dissipated heat from the cavity walls. This is achieved by plunging the cavities into a liquid helium bath, also known as a liquid helium phase separator (LHPS). The cavities were completely immersed in liquid helium at all times. If not fully immersed, a cavity may undergo a quench, that is, a partial or total loss of its superconducting state.

The other operating conditions are linked to any source of perturbations that may disturb the frequency of operation of cavities. Table II summarizes these sources. Because niobium is not infinitely stiff, any source of vibration in the liquid helium bath induces mechanical deformations and, therefore, frequency shifts. When oscillations are fast (> 100 Hz), the low-level radio frequency (LLRF) system control loop ensures the stability of the accelerating field in both amplitude and phase. However, this ability is limited by the power margin available from rf amplifiers. The frequency mismatch Δf with respect to the operation frequency f_0 of the machine can be written as

$$\Delta f = \frac{f_0}{2Q_L}\sqrt{\frac{P_{g\,\max}}{P_{g0}} - 1}, \tag{1}$$

where Q_L is the loaded quality factor, P_{g0} is the required rf power, f_0 is the resonant frequency, and $P_{g\,\max}$ is the maximum power delivered by the rf generator. For SPIRAL2, the values Q_L are 5.5×10^5 and 1.1×10^6 for type A and type B.

For SPIRAL2, because of the poor amplifier design margins, $P_{g\,\max}$ is clearly the limiting factor; for example, the threshold is already reached when experiencing helium pressure thermoacoustic oscillations in cryomodules/valve boxes. For the type B cryomodules, the limit in terms of pressure amplitudes was set to 1200 ± 5 mbar for 5 Hz pressure frequency modulations. When pressure oscillations are slow (< 1 Hz), it is the role of the frequency

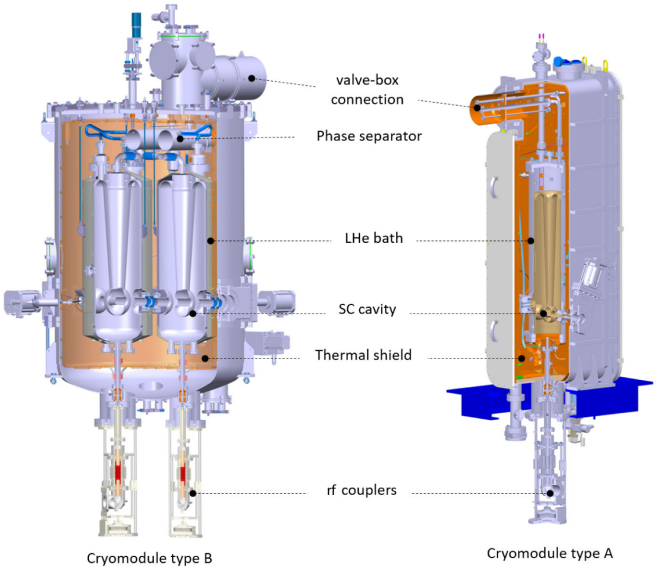


FIG. 1. 3D views for the two types of cryomodules with their principal components.

TABLE II. Main causes of perturbations that may affect rf operation of the SPIRAL2 cavities.

Source	Frequency	Correction
Lorentz force	~Static	FTS[a]
Helium P/L[b] cross coupling	~Hz	CS[c]
Helium CM[d] cross coupling	~Hz	CS
Cryogenic operation set point	~Hz	FTS
rf coupler temperature	$\sim 10^{-2}$ Hz	FTS
Other vibrations[e]	~Hz ⇒ ~100 Hz	LLRF

[a]Frequency tuning system.
[b]Pressure/level.
[c]Cryogenic system.
[d]Cryomodule.
[e]Includes thermoacoustics, vacuum pumps, vibrations, and helium turbulence.

TABLE III. Pressure sensitivities of SPIRAL2 cavities for $\delta\phi = \pi/12$ and $Q_L \sim 10^6$.

Cavities[a]	Cryomodules	S_p (Hz/mbar)	δP_{bath} ($\pm$mbar)
01	A01	−1.23	11.92
02	A02	−1.32	11.11
03	A03	−1.453	10.09
04	A04	−1.45	10.11
05	A05	−2.9	5.05
06	A06	−1.08	13.58
07	A07	−1.66	8.83
08	A08	−1.24	11.82
09	A09	−1.38	10.62
10	A10	−1.31	11.19
11	A11	−1.58	9.28
12	A12	−1.22	12.02
13	B01	−5.3	2.76
14	B01	−4.95	3
15	B02	−5.9	2.48
16	B02	−7.3	2
17	B03	−4.9	3
18	B03	−5.2	2.82
19	B04	−5.2	2.82
20	B04	−4.5	3.25
21	B05	−5.9	2.48
22	B05	−6.2	2.36
23	B06	−6.2	2.36
24	B06	−5.8	2.52
25	B07	−5.4	2.71
26	B07	−5.8	2.52

[a]Numbered by positions in the direction of the beam.

tuning system (FTS) to compensate cavities frequency deviations [2]. However, there are cases in which the FTS and LLRF correction capabilities are insufficient. High-amplitude liquid helium phase-separator pressure instabilities are a good example of phenomena that cannot be corrected by the FTS or compensated by the LLRF. This property is common to all low-bandwidth and high-quality-factor superconducting accelerating cavities, which are sensitive to micrometric mechanical deformations. This constraint can be expressed in terms of the frequency-pressure sensitivity S_p, a property that was measured during the qualification phase of the SPIRAL2 cavities [3]. Table III lists these properties. Based on the rf phase shift $\delta\phi$ between the incident power and the transmitted power, it is possible to translate this constraint in terms of the maximum acceptable pressure variation δP_{bath} of the LHPS as follows:

$$\delta P_{\text{bath}} = \frac{\delta f}{S_p} = \frac{f_0 \delta\phi}{\pi Q_L S_p}, \tag{2}$$

where δf is the admissible frequency shift, f_0 is the operating frequency or tuning frequency of the cavity, and S_p is the frequency sensitivity to pressure variations. The values of δP_{bath}, as calculated in Eq. (2), are listed in Table III for the measured S_p and $\delta\phi = \pi/12$.

III. THE ROLES OF THERMODYNAMIC MODELING

A. Model description

We have demonstrated how cryogenics can affect rf operation and, in turn, beam operation. The constraints highlighted in Sec. II depend on several localized and distributed systems and subsystems. One might consider a level-0 subsystem with its physical components as a given constraint that matches a single-process variable. For example, the cryomodule/valve box of level-1 subsystem would be composed of two level-0 subsystems for liquid helium level and helium pressure control. A level-2 subsystem corresponds to a given section of the LINAC. An even higher-level system would, in that case, include the entire cryoplant with complexity increasing as the number of parameters to be controlled increases. Knowledge of the different subsystems can provide several benefits. (i) Give a better visibility of the thermodynamic phenomena occurring in the LINAC. (ii) Avoid unwanted behaviors thanks to fast, reactive, and predictive controls.

For a level-1 subsystem simplified model corresponding to a single-cavity cryomodule with its valve box, the main components to be modeled are two valves for the helium inlet and outlet, a liquid helium phase separator, and a dynamic heater that mimics the behavior of the rf dynamic heat load. This simple model, documented in [4] and based on the Simcryogenics [5] library, permits a good prediction of the thermodynamic state of the system. The linearization of the physics model around the operational set point allows for efficient tuning of the valve controllers (see Sec. III B) and the generation of a real-time heat-load observer.

B. Optimized cryogenic control

One consequence of the proposed model is that the liquid helium level and phase-separator pressure can be predicted to an acceptable level. This, in turn, allows us to tackle one of the main issues that cryogenic operations have been experiencing, namely, helium pressure control. This difficulty is related to the fact that the time constant of the valves is on the order of a second, whereas helium pressure, for instance, can vary much faster (up to 20 Hz for nonperiodic variations and up to 100 Hz for thermoacoustic oscillations). At the beginning of the project, the corresponding process variables were managed using two separate and independent proportional integral (PI) controllers. The main problem with these controllers is that they are single-input/single-output controllers. Having a working model of this first-level-0 subsystem allowed us to synthesize and optimize a different model with multiple inputs/outputs. The new controllers we used are based on

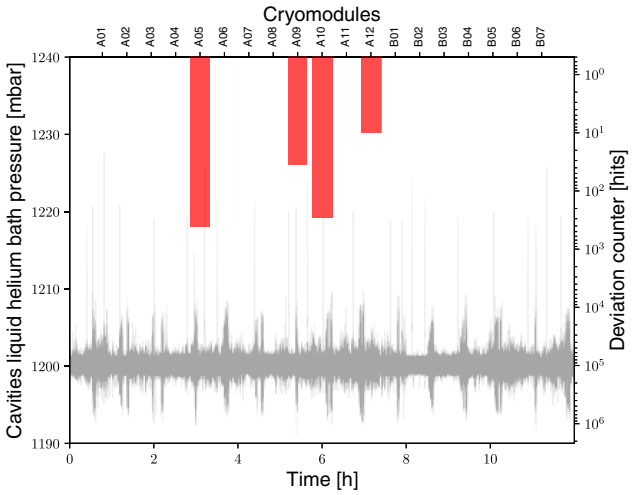


FIG. 2. Pressure variations overlay for the LINAC together with overlay of overshoot for deviations $\Delta(P) > \pm 5$ mbar during a time period of 12 h.

well known linear quadratic controllers (LQ) [6,7]. These controllers were validated on the LINAC through a separate test Programmable Logic Controller (PLC) before deployment in the main cryomodule PLCs.

Because liquid helium level control is less critical than pressure (see Sec. II), the main purpose of deploying the new control algorithm was to better control the pressure-induced frequency detuning of the cavities. When set to strictly withstand the S_p limit (see Table III), the PI controllers appeared to perform sufficiently well for type A cryomodules. For the rf regulation of type A cryomodules, the requirement was set to 5 mbar. Software surveillance to monitor pressure overshots higher than 5 mbar showed the advantage of a nonoptimized LQ on the LINAC with respect to an optimized PID for most cryomodules (see Fig. 2). After the LQ controller optimization at thermodynamic set points matching the required accelerating fields, the monitors did not show any overshoot. Today, optimized LQ controllers are routinely used in the operation of the SPIRAL2 LINAC.

C. Physics-based inference of cavities heat loads

State observers are essential tools for monitoring otherwise unmeasurable system states. These observers may be based on a combination of direct system measurements and model-based estimations. However, knowledge of a model offers the possibility of unlocking its hidden features. It also opens the door to the use of physics-oriented machine learning techniques for state observer generation. In the case of the thermodynamic model described in Sec. III A, a direct consequence is the ability to monitor the total heat load of the cryomodule/valve box subsystems. This relies on the knowledge of two main quantities: helium density variation $\dot{\rho}$ and internal energy dynamics $\dot{u}$ expressed as follows:

$$\dot{\rho} = \frac{\dot{m}_{\text{in}} - \dot{m}_{\text{out}}}{V_{\text{sep}}} \tag{3}$$

and

$$\dot{u} = \frac{\dot{m}_{\text{in}}(h_{\text{in}} - u) - \dot{m}_{\text{out}}(h_{\text{out}} - u) + Q_h}{\rho V_{\text{sep}}}, \tag{4}$$

where $\dot{m}_{\text{in}}$ and $\dot{m}_{\text{out}}$ are the input and output helium mass flows, respectively; V_{sep} is the liquid helium phase separator volume; h_{in} and h_{out} are the input and output enthalpies, u is the internal energy; and Q_h is the total heat load. Equations (3) and (4) allow for the direct recovery of the total dissipated heat load Q_h.

Such observers are inherently nonlinear, and their implementation in automation and control systems can be challenging. To overcome this challenge, linear state observers such as the extended Kalman filter [6,7] and the Luenberger observer [8] have been used. However, the resulting states are usually narrowband around the linearization point, that is, the operating conditions. Therefore, the final observer uses the nonlinear model to calculate the density ρ and internal energy u and the linearized model to calculate the matrix gain of the state observer (see [9] for more details on the gain matrix). Three strategies were tested on the model before its application to the real system: (1) slow observer, (2) fast observer, and (3) fast-filtered observer. The results in Table IV show that there is a trade-off. A fast-filtered observer was considered for the implementation of this system. In addition, calibrations under a wide range of operating conditions were performed to reduce errors.

Figure 3 shows the test implementation of a real-time heat-load observer in a SPIRAL2 cryomodule. The observer is challenged by applying different power variation shapes to a heater thermally coupled to a liquid helium phase separator. The test lasted for more than 40 h, and the heater power amplitudes varied between 0 and 10 W at a temperature of 4.2 K. The error related to the applied heater power was considered by calibrating the heater current with the actual heat loads measured by the liquid helium decay. The results in Fig. 3 show an error almost within the precision of the liquid helium decay technique. For our application, a heat load measurement by liquid helium decay takes up to 40 min depending on the power being

TABLE IV. Comparison of heat-load observers.

Observer type[a]	Response time (s)	Noise (W)
Slow	1200	0.5
Fast	50	12
Fast filtered[b]	100	2

[a]Generated with a Luenberger observer.
[b]A second-order low pass filter has been used here.

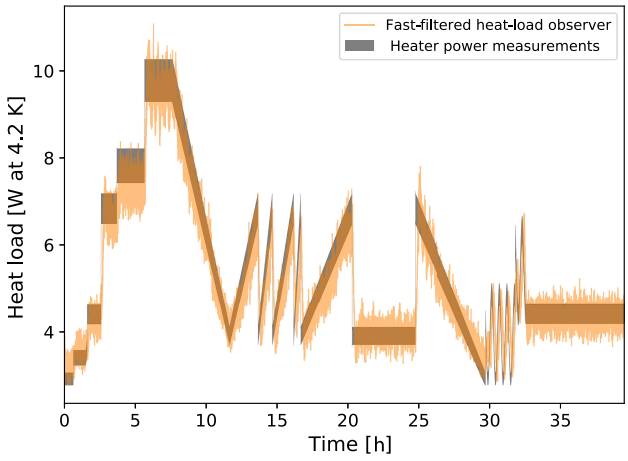


FIG. 3. Fast-filtered heat-load observer variation as heater power is varied with a specific pattern.

measured, and cannot be performed during rf or beam operation. The tested observer offers such *in situ* capability with noise varying between 0.6 and 1 W at 4.2 K and a time response of approximately 10 min. There is an important margin of improvement in the applied algorithms by adjusting the filters and time constants to the monitored behaviors. For example, a 10 min time response provides good monitoring of the absolute total heat load, while a time response of a few seconds provides insight into fast abnormal behaviors (relative variations) at the cost of increased noise. One example of abnormal behavior that has been detected is a virtual imbalance between the input and output helium mass flows of the cold box. In reality, the measured imbalance is a signature of the abnormal gas temperature at the output helium ports. This was caused by the method used to dampen the cryogenic thermoacoustic oscillations. The identification of the anomaly resulted in the application of a more suitable thermoacoustic damping solution (see Sec. IV A). Further studies on beam currents at different duty cycles are required to assess a more complete set of state observers. A complementary approach, for which a study is planned, will take advantage of beam diagnostics, vacuum gauges, and rf measurements to generate multiphysics observers. Another application under study is the *in situ* measurement of the quality factors Q_0 of the accelerating cavities and the identification of possible degradation causes (field emitters, surface resistance degradation, etc.) [10,11]. These applications are coupled with complementary ongoing studies that leverage machine learning techniques for advanced diagnostics.

D. Machine learning-based inference of cavities heat loads

Artificial intelligence has revolutionized numerous scientific fields, and particle accelerator applications are no exception, increasingly benefiting from advances in deep learning techniques [12]. Among existing model architectures, neural networks have demonstrated significant potential in overcoming the limitations of traditional physics-based observers. However, these models depend on access to large volumes of high-quality data. To generate such datasets, a series of machine studies were conducted by inducing controlled heat loads using electric heaters thermally connected to the cavity phase separators. The training phases followed a gradual variations in the induced heat loads from 0 to 24 W, with step durations and amplitudes ranging from 1 to 15 min and 1 to 10 W. Several neural network architectures were evaluated, including multilayer perceptrons (MLP) [13], one-dimensional convolutional neural networks (1D-CNN) [14,15], and long short-term memory networks (LSTM) [16] with (LSTMa) and without Luong attention [17], under various selections of input variables. An architecture called stacking [18], created using pretrained models, was trained using a different training set. The input sequences passed through each pretrained model, and their outputs were concatenated before passing into the feedforward layers. No dropout techniques were added because the tests did not show any signs of overfitting. During the training of the stacking model, the pretrained models were frozen, and only the feedforward layers were trained. All models were trained with mean squared error as the loss function, Adam algorithm [19] as the optimizer, and a batch size of 256.

For each heat load step, 10-timestamp sequences were created without overlap and added to the training (40% for MLP, CNN, LSTM, and LSTMa models +40% for the

TABLE V. Statistics of residuals (in W) and R^2 for models trained and evaluated on A08 cryomodule 2022 data cooled at 4.2 K.

	MLP	CNN	LSTM	LSTMa	Stacking
Mean	−0.010	−0.036	−0.011	−0.026	−0.009
Standard deviation	0.514	0.378	0.415	0.379	0.348
First quartile	−0.218	−0.191	−0.173	−0.185	−0.142
Median	−0.007	−0.032	−0.004	−0.018	−0.004
Third quartile	0.211	0.133	0.173	0.135	0.133
Interquartile range	0.430	0.325	0.346	0.320	0.275
R^2	0.993	0.996	0.996	0.996	0.997

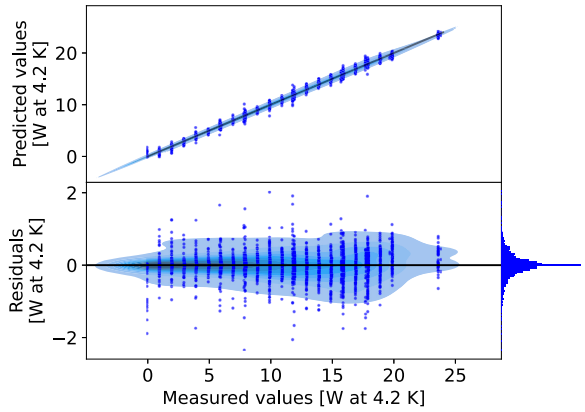


FIG. 4. Heater-induced heat load predictions with the stacking model on A08 cryomodule 2022 data at 4.2 K. Top: predicted versus measured values with kernel distribution; bottom: residuals versus measured values with kernel distribution and distribution of residuals. The R^2 score is 0.997.

stacking model), validation (10%), and test (10%) sets. The neural networks were created, trained, and evaluated on a personal computer without a graphical processing unit (GPU). This choice follows the assumption that a lightweight LSTM model would not benefit significantly from GPU acceleration, as the data transfer between the RAM and GPU VRAM often becomes a bottleneck in such cases. This bottleneck disappears when the number of parallelizable computations increases sufficiently to offset the data transfer cost. However, this assumption has not been evaluated in our case. Further studies could benefit from GPU acceleration.

The models were evaluated by calculating the difference between predicted and measured heat loads, also called residuals, and the $R^2 = 1 - \frac{\sum_{i=1}^{n}(y_i - \hat{y}_i)^2}{\sum_{i=1}^{n}(y_i - \bar{y})^2}$ score. Table V presents the statistics of residuals and R^2 for these models trained and evaluated on A08 cryomodule 2022 data with the following features as input: helium pipe inlet and outlet temperatures, inlet and outlet valve openings, and the level and pressure of the liquid helium bath.[4] The models were tested using the same test set. Figure 4 shows the heat loads at 4.2 K predicted using the stacking model and this selection of input variables. The computation time required to predict 2841 values is approximately 0.4 s.[5]

Further studies with randomly generated heat load steps (amplitude and duration) should be conducted. The data can be divided chronologically, and consequently, the length of the sequences can be increased. This would likely lead to improvements in the robustness and accuracy of the models during the transients. Uncertainty estimation methods [20] could also be explored to enhance confidence in model predictions.

IV. FROM CRYOGENIC TO BEAM OPERATION

A. Thermoacoustics: Hints, effects, and ways out

SPIRAL2 has served as a valuable platform for investigating and addressing the challenges posed by cryogenic thermoacoustic oscillations (TAOs) [21]. In the present study, these oscillations were observed at multiple locations across a frequency range of 5–100 Hz. Although the TAOs in the main phase separator of the cryoplant have been effectively damped using an optimized capacitance, those occurring within the LINAC have proven to be more complex to mitigate. These oscillations, originating from the cryogenic valve boxes and other components of the cryomodules, disrupt stable LINAC operation by inducing pressure and temperature fluctuations, cavity detuning, and increased heat loads. Initial investigations identified the presence of TAOs within the cavities through fluctuations in the rf signals and pressure sensor data, excluding external mechanical vibrations as the root cause.

This challenge provided an opportunity to utilize SPIRAL2 as a testbed for studying distributed and

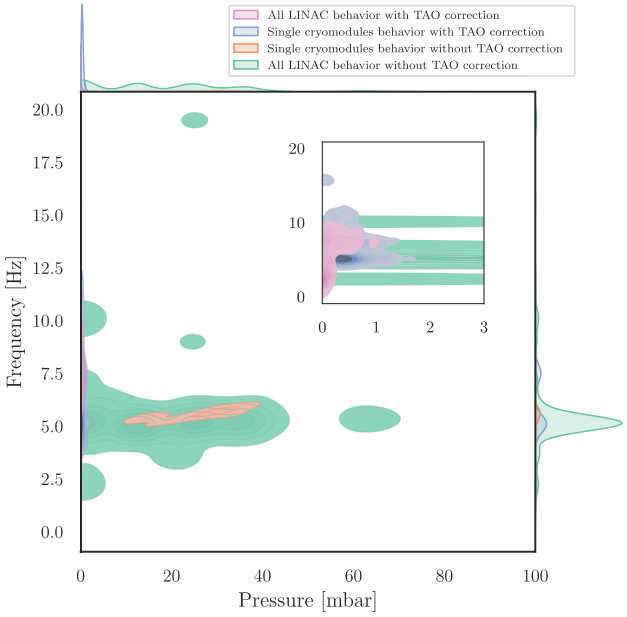


FIG. 5. Kernel density distribution of resonance frequencies obtained from Fourier analysis of detected thermal acoustic oscillations (TAOs) along the LINAC. Each point corresponds to a single resonance identified at a given cryomodule or across the entire LINAC, with pressure amplitude and frequency extracted from the oscillatory signals.

[4]These temperature sensors are located on the outside of the pipes through which the helium flows. The temperatures and valve openings were normalized using the values at 0 and 20 W induced heat load; for the level and pressure of the helium bath, deviations from the set points were used.

[5]Operating system: Ubuntu 22.04.5 LTS, Available RAM: 15 GB, CPU: Intel i5-1235U, TensorFlow version: 2.15.0, Programming language: Python (3.10.12).

interconnected cryogenic thermoacoustic oscillators, analyzing their impedance properties, and evaluating various damping strategies. Two experimental approaches were employed. First, the oscillation amplitudes and frequencies were characterized using nominal operating conditions. Simultaneous piezoelectric measurements of the relative pressure in the liquid helium phase separators of the cavities facilitated precise time- and frequency-domain analyses, resulting in the first thermoacoustic map of an operational superconducting LINAC (Fig. 5). Their analysis indicated that local factors predominantly influenced oscillations when confined to a single cryomodule, whereas more complex cross-coupling effects emerged during simultaneous oscillations across multiple cryomodules.

Second, an adjustable resistance, inductance, and capacitance (RLC) resonator was employed to investigate the acoustic impedance and evaluate the damping strategies. Several damping solutions have been tested, including short-circuit lines, buffers, pistons, and RLC resonators. Among these, the short-circuit lines connecting the 5 K helium gas return circuit to the cavity phase separators demonstrated the highest damping efficiency. However, this approach introduces side effects such as condensation and valve instability. Adjusting the exchange flow rate between the circuits effectively mitigated these side effects of the heat pump.

One notable advantage of the SPIRAL2 LINAC setup is its ability to actively induce or suppress thermoacoustic oscillations, thereby functioning as a unique laboratory for studying and mitigating these phenomena in superconducting accelerators.

B. Heat load measurements and automatic rf load compensation

Obtaining a thermal image of the LINAC under nominal operating conditions is an important step in ensuring reliable cryogenic, rf, and beam operations. In a simplified thermodynamic-electrical analogy, the LINAC can be considered an unevenly distributed parallel impedance. The cold box functions as a generator. The cryomodules, mounted in parallel, are then operated at the same voltage (or helium pressure) but are subject to different currents (helium mass flows) depending on their characteristic impedances (heat loads). A cryomodule with a higher heat load can then unbalance the distribution and deprive a neighboring cryomodule of part of the liquid helium flow or cause significant instabilities. To avoid this type of problem, the helium flow is equally distributed between the two arms of the LINAC (see Fig. 7) and between the different cryomodules. Figure 6 shows a snapshot of the heat-load balancing for the SPIRAL2 LINAC. This is done owing to the heaters in the cryomodules, allowing for artificial[6] heat load compensation.

[6]Not induced by rf or beam loading.

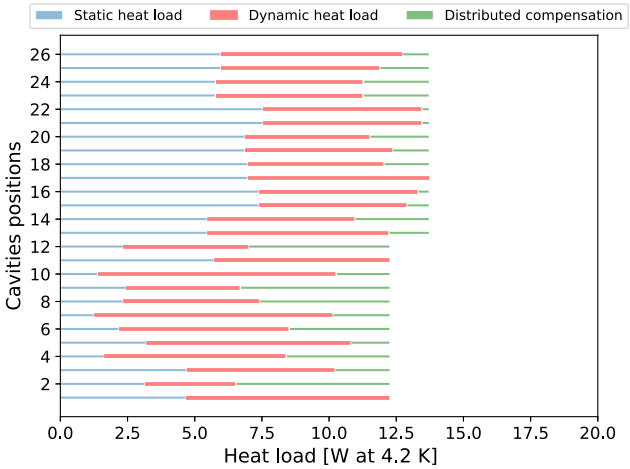


FIG. 6. Static, dynamic, and distributed heat load compensation. The figure shows the actual measurements and compensations applied to the SPIRAL2 LINAC. Abnormal features are hidden for a better visibility and are shown in Fig. 8.

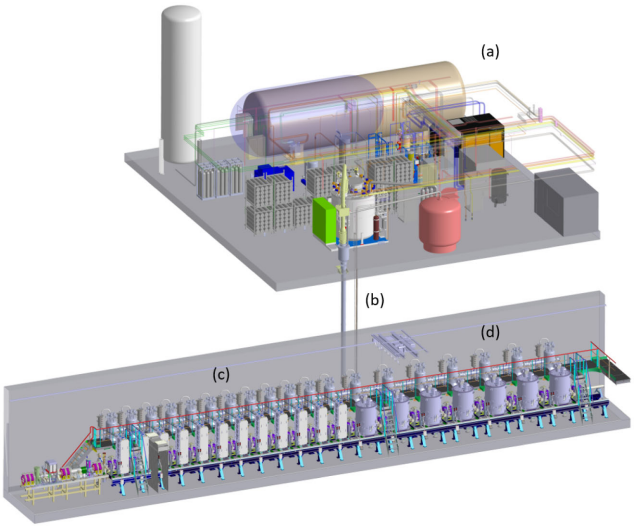


FIG. 7. (a) Cryoplant, (b) cryogenic distribution line, (c) and (d) LINAC cryomodules A and B, respectively.

For each cryomodule, the total heat load P_{total} can then be expressed as

$$P_{\text{total}} = P_d + P_s + P_{\text{comp}}, \tag{5}$$

where P_d denotes the dynamic heat load, P_s denotes the static heat load, and P_{comp} denotes the compensation heat load for a given cryomodule.

If a reference heat load P_{ref} is considered as the maximum cryomodule heat load in the LINAC without compensation, the compensation heat load for the other cryomodules can be expressed as

$$P_{\text{comp}} = P_{\text{ref}}c - P_s - P_d, \tag{6}$$

where $c = 1$ for type B cryomodules and $c = 7/12$ for type A cryomodules (see the introduction for types A and B cryomodules).

One consequence of this compensation strategy is that the heat load remains constant at all times. As the dynamic heat load is variable and depends mainly on the accelerating field of the cavities, knowledge of the thermal image of the LINAC as a function of the accelerating field is important. To gain this knowledge, systematic measurements of thermal dissipation were performed at different accelerating fields for each cavity. For this purpose, the liquid helium variation method was used, wherein the inlet valve was closed and the outlet valve was kept under pressure regulation. The decay of the liquid helium level was measured. The heat load is given by

$$P_{\text{thermal}} = \frac{dV}{dt}\rho C_l, \tag{7}$$

where V is the liquid helium volume, t is the time, ρ is the liquid helium density at liquid helium pressure, and C_l is the latent heat of the liquid helium. In practice, the phase separator volume, as a function of the liquid helium probe measurement, was extracted from 3D models of the cryomodules. ρ was directly calculated from the pressure process value using the CoolProp Python library [22]. Finally, $\frac{dV}{dt}\rho$ was fitted. The entire measurement procedure was automated and integrated into the command control. The resulting thermal image of the LINAC is shown in Fig. 8 top axis scale heatmap.

In the absence of dynamic compensation within the cryomodules or helium mass flow balance between the different cryomodules, the dynamic thermal dissipation P_d for one cavity can be expressed as follows:

$$P_d = P_r + P_{\text{em}} \sim \frac{E_{\text{acc}}^2}{Q_0 K^2}, \tag{8}$$

where P_{em} denotes the extra losses due to field emission (x-ray production caused by electron acceleration in the rf field and deceleration in the cavity walls). P_r represents the effects of the cavity wall surface resistance, Q_0 is the unloaded quality factor, and K is a geometrical constant. Equation (8) is valid only if P_{em} can be neglected.

For SPIRAL2, the accelerating cavities operate at accelerating fields lower than 7 MV/m, where the field emission effects can be neglected. At these accelerating fields, the so-called quality factor drop due to field emission can be also neglected. This leads to a simple approximated second-order polynomial dependence of the heat load on the acceleration field, as follows:

$$P_d = AE_{\text{acc}}^2, \tag{9}$$

with $A = 1/Q_0K^2$.

Figure 9 shows the measurements of the total heat loads of the cavities as a function of the accelerating fields fitted to Eq. (9). Apart from the cavity 11 anomaly (discussed in Sec. IV C 1), two groups corresponding to the two cryomodule families can be clearly differentiated. The main reason for this is that the two groups exhibited different static heat loads.

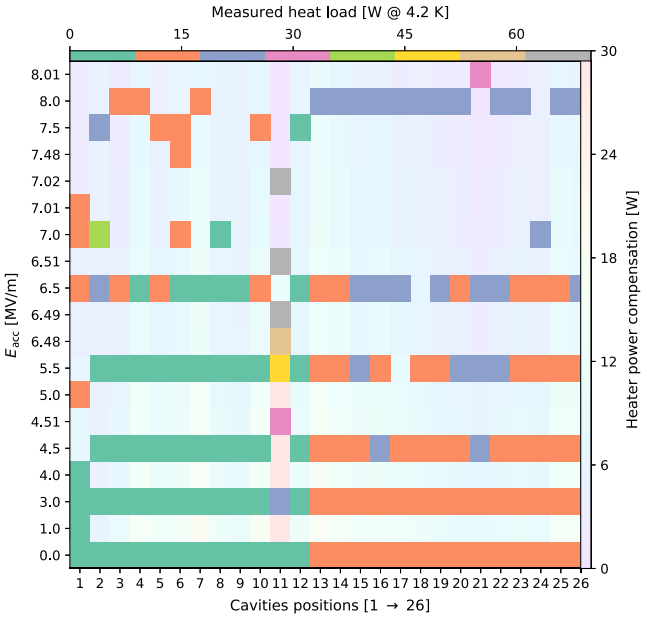


FIG. 8. Heatmap of the measured LINAC thermal image at different accelerating fields (darker colors) together with the fitted continuous compensation power (lighter colors).

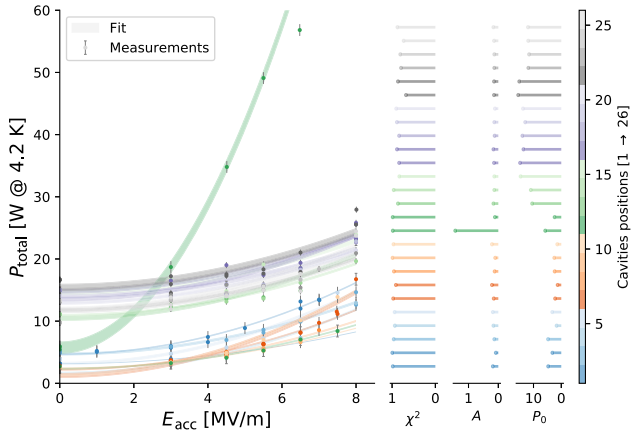


FIG. 9. Measured and fitted heat load dissipation of the SPIRAL2 cavities as a function of the accelerating gradients. P_0 represents the heat load dissipation at zero accelerating gradient and χ^2 the goodness-of-fit.

Consequently, the heater compensation power required to maintain a constant and balanced heat load when the accelerating field varies can be expressed as

$$P_{\mathrm{comp}} = A(E^2_{\mathrm{acc,nom}} - E^2_{\mathrm{acc,meas}}) + P_{\mathrm{dist}}, \tag{10}$$

where $P_{\mathrm{dist}} = P_{\mathrm{ref}}.c - P_s$ [Eq. (6)]. The calculated power compensation heatmap for $E_{\mathrm{acc,nom}} = 6.5$ MV/m is shown in Fig. 8.

C. *In situ* diagnostics of cavity anomalies

When anomalies arise, Eq. (9) is no longer valid, and neglected terms must be fully accounted for. In Eq. (8), Q_0 is no longer constant [10] and is expressed as

$$Q_0 = \frac{G}{R_s}, \tag{11}$$

where G is a geometric factor, and R_s is the surface resistance, expressed by

$$R_s = R_{\mathrm{res}} + R_{\mathrm{BCS}}, \tag{12}$$

where R_{res} is the residual surface resistance and R_{BCS} is the BCS[7] resistance. R_{res} is, in turn, expressed as

$$R_{\mathrm{res}} = R_0 + E_{\mathrm{acc}}R_{\mathrm{acc}}, \tag{13}$$

where R_0 is the residual resistance at the null field and R_{acc} is the sensitivity of the resistance to the accelerating field E_{acc} [23].

In Eq. (12), R_{BCS} is a function of the energy gap, temperature, frequency, and maximum magnetic field. Regarding electronic field emission, P_{em} can be expressed as

$$P_{\mathrm{em}} = \alpha J_{\mathrm{em}}, \tag{14}$$

where α is a constant proportional to surface emission and J_{em} is the Fowler-Nordheim current density [24].

From Eqs. (5), (8), (13), and (14), it follows for a given cavity, temperature, and frequency:

$$P_{\mathrm{raw}} = \frac{E^3_{\mathrm{acc}}R_{\mathrm{acc}}}{G * K^2} + \frac{E^2_{\mathrm{acc}}(R_0 + R_{\mathrm{BCS}})}{G * K^2} + \alpha J_{\mathrm{em}} + P_0, \tag{15}$$

where P_{raw} is the total uncompensated power dissipation. An important consequence is that heat load monitoring across a wide range of accelerating fields can allow the diagnosis and differentiation of various symptoms of abnormal cavity behaviors. Measurement campaigns allow the monitoring of parameters such as α, the characteristic of the field emitter size, or R_{res} for the surface resistance. One example is shown for the A02 cryomodule in Fig. 10, where the blue curve represents the regular behavior typical of SPIRAL2 cavities. In the same figure, above 6 MV/m, the heat load exhibits a shape typical of field emission. A consequence of this abnormal behavior was the limitation of the operation of this cavity to low accelerating gradients. This choice may not be possible for high-beta cavities or cavities at the junction of high- and low-beta cavities. This case is discussed in Sec. IV C 1.

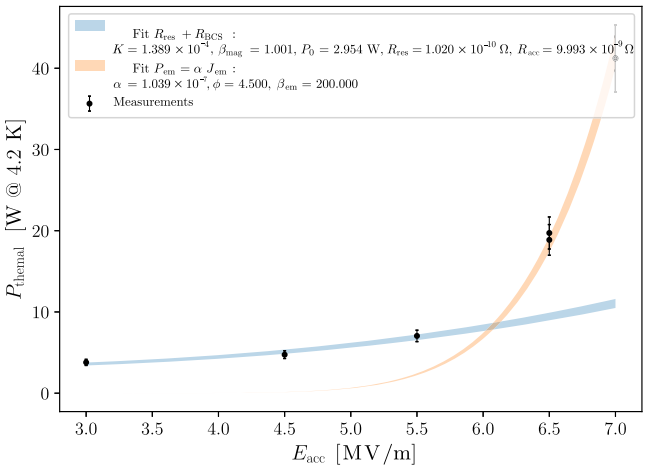


FIG. 10. A02 cavity heat load dissipation as a function of the accelerating gradient with fits of the surface resistance and the field emission contributions. ϕ is a fitted constant, α is proportional to the surface emission, and β_{em} is a coefficient that multiplies the electric field.

1. The special case of cryomodule A11

The A11 cavity was the first to be assembled and qualified at the CEA/IRFU, but it was also the last to use a Helicoflex™ vacuum seal for the removable bottom of the cavity (see Fig. 11). These seals generated more heat load than expected and were replaced in all other type A cryomodules by a copper ring and two indium wires, which acted as both vacuum and rf seals. In addition, the rf power coupler used was prepared and conditioned using non-optimized procedures [25], which were then implemented

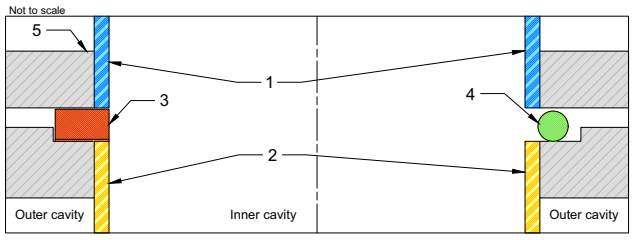


FIG. 11. Cavity bottom sealing techniques used for A11 cryomodule (right part) and all other type A cryomodules (left side). Legend: (1) inner cavity walls—bulk niobium part; (2) inner cavity walls—copper part; (3) indium-copper seal (other type A cryomodules); (4) Helicoflex™ seal; and (5) stainless steel flange.

[7]Bardeen-Cooper-Schrieffer resistance.

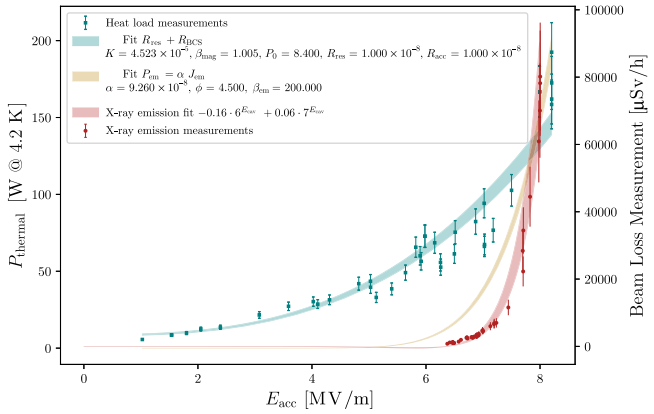


FIG. 12. A11 cavity heat load dissipation measurements (green points) as a function of the accelerating gradient (left axis) with both the surface resistance (green) and the field emission (yellow) contributions fitted separately. The right axis measurement shows x-ray emission measurements (red) as a function of the accelerating gradient. β_{mag} is the magnetic field enhancement factor and β_{em} is the electric field emission enhancement factor.

for all other cryomodules of the SPIRAL2 accelerator. The first qualification of the cavities on its test stand showed abnormal behavior typical of field-emitting cavities with heat loads up to 40 W at 4.2 K and 6.5 MV/m. Helium processing [26] has been applied and has been efficient enough to cure this cavity and bring its heat load down to 20 W at 4.2 K and 6.5 MV/m, well within the specifications.

In situ investigations. However, the first operation in the LINAC showed a completely different behavior. The bottom temperature of the cavity showed a different dependence on the accelerating gradients, with a jump of approximately 6 MV/m (see Fig. 13). In 2020, a dedicated machine study was conducted to localize

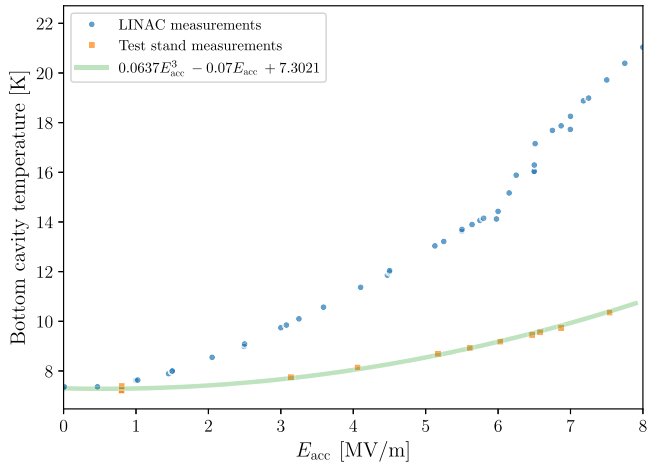


FIG. 13. A11 cavity's bottom temperature measurement in the LINAC and in the test stand.

abnormal heat loads. Cryomodules of the A family are equipped with two helium level sensors that independently monitor the helium level inside the cavity stem and between the helium vessel and outer cavity walls (see [27] for a detailed description of the cavity geometries). The main conclusion of the machine study was that the thermal losses were located either at the bottom of the cavity, on the rf coupler, or on the outer walls of the coaxial cavity. Interestingly, abnormal dissipation did not occur in the main rf loss areas (i.e., the top of the stem and top torus of the cavity). Combined measurement of heat loads from 1 to 8 MV/m (see Fig. 12) showed three main regions of field dependence losses:

(1) The first region is below 5.5 MV/m, where the thermal losses seem to be dominated by surface resistance losses. The green curve fit in Fig. 12 shows that the surface resistance R_{res} and resistance field sensitivity R_{acc} are up to 2 orders of magnitude higher than those of the other cryomodules. Two main conclusions can be drawn from this observation. First, the high sensitivity to the field points toward a conductive behavior typical of normally conductive materials. Second, a significant degradation in the surface resistance was observed. The latter is an effective value that considers three contributions: the surface resistance of the superconducting bulk niobium (typically $\sim n\Omega$), the surface resistance of copper (bottom part of the cavity), and finally, an interface region between the two parts of the cavity centered around the sealing (see Fig. 11), but possibly expanding and transiting part of the Nb region to its normal state. However, these contributions are weighted by the geometric distribution of the magnetic field, which is close to its minimum in the sealing regions. A discontinuity in the conductive inner wall region of the cavity can cause rf field leaks that can drastically increase the rf losses at the interface region. (2) A second region between 5.5 and 6.5 MV/m where we can see a jump in the temperature of the bottom of the cavity and where the measured heat load seems to flatten. (3) The third region is above 7 MV/m, where the thermal load is dominated by the field emission. In this region, the heat load is correlated with the x-ray emissions measured using dedicated beam loss monitors (see Fig. 12). This behavior is not problematic because the cavity is not operated above 6.5 MV/m.

The three regions described above may correspond to transitions in the liquid helium flow regime owing to an increased heat load. The first region likely represents a single-phase liquid flow. The second is the onset of nucleate boiling, where small vapor bubbles begin to form on heated surfaces. Finally, the third region is dominated by the Leidenfrost effect [28]. In this regime, also known as the film boiling transition, a very high heat flux leads to the formation of an insulating vapor layer between the liquid helium bath and the cavity surface, significantly reducing heat transfer efficiency and exacerbating the temperature rise.

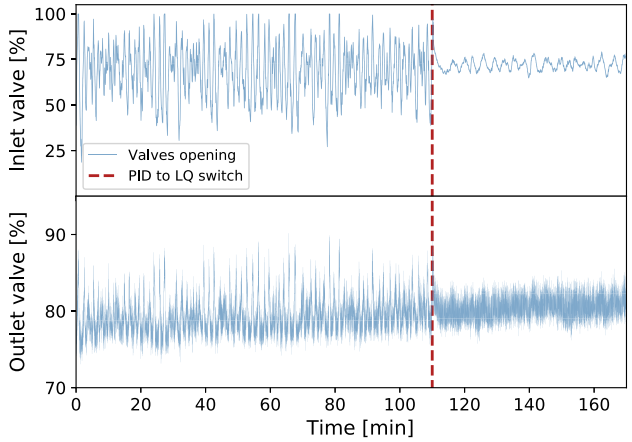


FIG. 14. A11 cryomodule helium inlet and outlet valve openings before (PID control) and after applying the model-based (LQ) control. These measurements were done before changing the CV of the outlet valve.

Operation constraints and solutions. Given the obtained results, the only way to lower the abnormal heat load of the cryomodule is to disassemble it completely and reprocess the cavity in a clean room using a power coupler prepared using the standard optimized procedures and replacing the Helicoflex™ seal with the standard copper + indium assembly. Considering the lack of spare cryomodules and the unavailability of a dedicated test bench for cryomodules at GANIL, this operation was postponed to a later date. The issue with a cryomodule dissipating so much is that the output helium flow is close to the acceptable limits of the piping geometries. Consequently, the inlet and outlet valve openings exceeded 75% when the cavity was operated at 6.5 MV/m. Apart from having valves that operate close to their nonlinear range (which adds instability to their control), such openings increase the sensitivity of the helium bath to its surrounding environment (neighboring cryomodules and cryodistribution) and the cross coupling between liquid helium regulation and pressure regulation. The model-based control detailed in Sec. III B allows for the effective overcoming of these issues by stabilizing the valves around an optimized operation set point (see Fig. 14). The applied set point[8] was chosen to account for the heat load increase during the cavity voltage ramp-up without destabilizing the cavity. As a compensatory measure, the outlet cryogenic valve plug was replaced to increase its inner flow coefficient (CV) to a value close to its maximum design capability.[9] This provides a larger margin for operation, particularly in the case of an increase in the heat load. The operation of cavity A11 in 2021 was satisfactory, with stable behavior and no increase or decrease in heat load. However, the gain margin remained low. A significant degradation of the heat load would require additional measures, such as low accelerating field operation[10] or replacement with a drift tube to allow for repair.

D. Next steps: Making operation smarter

The cryogenic process at SPIRAL2 relies on several PLC-based control systems [29]. These systems drive the operation and other related systems, such as the isolation vacuum and mechanical frequency tuning of the cavities. The previously described linear quadratic regulators were pretuned at a given set point in a separate MATLAB framework. The parameters are then embedded in the command-control PLCs. Day-to-day operations may require operators to retune the LQ regulator parameters. For this purpose, a new human-machine interface was developed. This interface allows regulation specialists to (i) recompute the linearization of the cryomodule models around a new set point, (ii) tune the heat-load observers' and LQ controllers' parameters (weights, filters, dynamics), (iii) simulate the performance of the regulators, (iv) switch between several tuning presets, and (v) transfer the model and regulation matrix to the cryomodules PLCs.

The linearized models of the cryomodules had a certain bandwidth around the calculated set points. The observers can monitor heat load deviations from a given set point. The next step would be to preload several linearized models around different heat loads in the PLCs and manually switch the presets upon detection of an important deviation. As the estimated heat load data produced by the observers become more reliable, it might be possible to exploit them to provide more explicit information, such as warnings, alarms, or even to automate the relinearization process of the cryogenic model used to compute the observers and LQ controllers. A further step, currently under development, would be to learn the nonlinear cryomodule models using machine learning techniques with the twin cryogenic model and operation data for increased precision. The models would then be embedded in their lightweight versions[11] into the control system.

V. CONCLUSION

SPIRAL2 has proven the value of advanced cryogenic and superconducting technologies for ensuring the reliable operation of superconducting LINAC. The transition from commissioning to full operation has highlighted innovative solutions to complex challenges, such as overcoming thermoacoustic oscillations and using machine learning

[8]The set point is an optimized heat load around which the model is linearized before extracting the valve control matrices.

[9]CV has been increased from 1.5 to 3.2 after plug replacement.

[10]This could mean to move the cryomodule to a different position in the beginning of the LINAC where the required accelerating gradients for the target current and energies are lower.

[11]See Deepgreen and LightML.

for cavity diagnostics. By incorporating thermodynamic models and optimized control systems, the facility achieves both stability and efficiency even under demanding conditions.

As the focus shifts toward smarter and more adaptive systems, advanced techniques such as drift surveillance and automatic regulator calibration are planned for integration into command-and-control systems. However, a superconducting linear accelerator comprises interconnected and interdependent subsystems, including radio frequency (rf), beam diagnostics, and cryogenics. This interdependency presents opportunities for smarter and more reliable operations through the use of generalized state observers and advanced diagnostic tools.

ACKNOWLEDGMENTS

This work has been funded by "Region Normandie" as well as the city of Caen, CNRS and CEA.

DATA AVAILABILITY

The data that support the findings of this article are not publicly available. The data are available from the authors upon reasonable request.

[1] A. Ghribi, P.-E. Bernaudin, A. Vassal, and F. Bonne, Status of the SPIRAL 2 LINAC cryogenic system, Cryogenics **85**, 44 (2017).

[2] D. Longuevergne, N. Gandolfo, G. Olry, H. Saugnac, S. Blivet, G. Martinet, and S. Bousson, An innovative tuning system for superconducting accelerating cavities, Nucl. Instrum. Methods Phys. Res., Sect. A **749**, 7 (2014).

[3] P. Bernaudin, R. Ferdinand, P. Bosland, C. Marchand, D. Longuevergne, G. Olry, and Y. G. Martínez, SPIRAL2 cryomodule production result and analyses, in *Proceedings of the 27th Linear Accelerator Conference-LINAC14* (2014), pp. 814–818, https://inspirehep.net/literature/1363525.

[4] A. Vassal, F. Bonne, A. Ghribi, F. Millet, P. Bonnay, and P. Bernaudin, Dynamic modeling and control of the SPIRAL2 cryomodules, IOP Conf. Ser. **502**, 012111 (2019).

[5] F. Bonne, S. Varin, A. Vassal, P. Bonnay, C. Hoa, F. Millet, and J.-M. Poncet, Simcryogenics: A library to simulate and optimize cryoplant and cryodistribution dynamics, IOP Conf. Ser. **755**, 012076 (2020).

[6] L. A. McGee, S. F. Schmidt, L. A. Mcgee, and S. F. Sc, *Discovery of the Kalman Filter as a Practical Tool for Aerospace and Industry* (National Aeronautics and Space Administration, Ames Research, Citeseer, Moffett Field, CA, 1985).

[7] L. Torres, J. Jiménez-Cabas, O. González, L. Molina, and F.-R. López-Estrada, Kalman filters for leak diagnosis in pipelines: Brief history and future research, J. Mar. Sci. Eng. **8**, 173 (2020).

[8] M. Zeitz, The extended Luenberger observer for nonlinear systems, Syst. Control Lett. **9**, 149 (1987).

[9] A. Vassal. Etude d'un réseau cryogénique multi-clients pour SPIRAL2, Ph.D. thesis, University of Caen Normandie, Normandie, 2019.

[10] W. Weingarten, Field-dependent surface resistance for superconducting niobium accelerating cavities, Phys. Rev. ST Accel. Beams **14**, 101002 (2011).

[11] D. Longuevergne, Geometrical corrections for accurate fitting of the field dependent surface resistance for superconducting accelerating cavities, Nucl. Instrum. Methods Phys. Res., Sect. A **910**, 41 (2018).

[12] A. Ghribi, K. Cassou, B. Dalena, A. Eichler, H. Guler, A. K. Mistry, A. Oeftiger, T. Shea, G. Valentino, and C. P. Welsch, Artificial intelligence for advancing particle accelerators, Europhys. News **56**, 15 (2025).

[13] D. E. Rumelhart, G. E. Hinton, and R. J. Williams, Learning representations by back-propagating errors, Nature (London) **323**, 533 (1986).

[14] Y. Lecun, L. Bottou, Y. Bengio, and P. Haffner, Gradient-based learning applied to document recognition, in *Proceedings of the IEEE* (IEEE, New York, 1998), Vol. 86, pp. 2278–2324),10.1109/5.726791.

[15] Y. Zheng, Q. Liu, E. Chen, Y. Ge, and J. L. Zhao, Time series classification using multi-channels deep convolutional neural networks, in *Web-Age Information Management*, edited by F. Li, G. Li, S.-W. Hwang, B. Yao, and Z. Zhang (Springer International Publishing, New York, 2014), pp. 298–310.

[16] S. Hochreiter and J. Schmidhuber, Long short-term memory, Neural Comput. **9**, 1735 (1997).

[17] M.-T. Luong, H. Pham, and C. D. Manning, Effective approaches to attention-based neural machine translation, arXiv:1508.04025.

[18] D. Wolpert, Stacked generalization, Neural Netw. **5**, 241 (1992).

[19] D. P. Kingma and J. Ba, Adam: A method for stochastic optimization, arXiv:1412.6980.

[20] J. Gawlikowski, C. R. N. Tassi, M. Ali, J. Lee, M. Humt, J. Feng, A. Kruspe, R. Triebel, P. Jung, R. Roscher, M. Shahzad, W. Yang, R. Bamler, and X. X. Zhu, A survey of uncertainty in deep neural networks, arXiv:2107.03342.

[21] A. Ghribi, M. Aburas, A. Alhaffar, P.-E. Bernaudin, P. Duthil, M. Nemer, and J.-P. Thermeau, Cryogenic thermoacoustics in the SPIRAL2 LINAC, Cryogenics **124**, 103487 (2022).

[22] I. H. Bell, J. Wronski, S. Quoilin, and V. Lemort, Pure and pseudo-pure fluid thermophysical property evaluation and the open-source thermophysical property library CoolProp, Ind. Eng. Chem. Res. **53**, 2498 (2014).

[23] D. Longuevergne, Etude et test d'un module accélérateur supraconducteur pour le projet Spiral2, Ph.D. thesis, Université Paris Sud-Paris XI, 2009.

[24] R. Fowler and L. Nordheim, Electron emission in intense electric fields, Proc. R. Soc. A, **119**, 173 (1928).

[25] Y. G. Martínez, M. Baylac, P. Boge, T. Cabanel, P. De Lamberterie, J. Giraud, F. Vezzu, F. Chatelet, C. Joly, J. Lesrel *et al.*, Final results of power conditioning of

SPIRAL2 couplers, Nucl. Instrum. Methods Phys. Res., Sect. A **870**, 37 (2017).

[26] J. Knobloch and H. Padamsee, Explosive field emitter processing in superconducting rf cavities, Part. Accel. **61**, 169 (1998), https://inspirehep.net/literature/492555.

[27] P. Bernaudin, R. Ferdinand, P. Bosland, G. Olry, and Y. G. Martínez, Assembling, testing and installing the SPIRAL2 superconducting LINAC, in *Proceedings of the 4th International Particle Accelerator Conference, IPAC-13* (Joint Accelerator Conferences Website, Geneva, Switzerland, 2013), pp. 3752–3754.

[28] J. Walker, Boiling and the leidenfrost effect, in *Fundamentals of Physics*, edited by D. Halliday, R. Resnick, and J. Walker (Wiley, 2010), https://www.reed.edu/physics/332/pdf/Leidenfrost.pdf.

[29] A. Trudel, P. Bonnay, G. Duteil, A. Ghribi, and Q. Tura, Control system of the SPIRAL2 superconducting LINAC cryogenic system, in *Proceedings of the ICALEPCS'21, International Conference on Accelerator and Large Experimental Physics Control Systems No. 18* (JACoW, Geneva, Switzerland, 2022), pp. 382–386.